Charting the landscape of Bardeen–Cooper–Schrieffer superconductors in experimentally known compounds

Marnik Bercx^{1,*}, Samuel Poncé^{2,3,**}, Yiming Zhang², Giovanni Trezza⁴, Amir Ghorbani Ghezeljehmeidan⁵, Lorenzo Bastonero⁶, Junfeng Qiao⁷, Fabian O. von Rohr⁸, Giovanni Pizzi¹, Eliodoro Chiavazzo⁴, Nicola Marzari^{1,6,7}

³WEL Research Institute, Avenue Pasteur 6, 1300 Wavre, Belgium.

⁴Department of Energy, Politecnico di Torino, Italy.

⁵Electronic Components, Technology and Materials (ECTM), TU Delft, The Netherlands.

Abstract

We perform a high-throughput computational search for novel phonon-mediated superconductors, starting from the Materials Cloud 3-dimensional structure database of experimentally known inorganic stoichiometric compounds. We first compute the Allen-Dynes critical temperature (T_c) for 4533 non-magnetic metals using a direct and progressively finer sampling of the electron-phonon couplings. For the candidates with the largest T_c , we use automated Wannierizations and electron-phonon interpolations to obtain a high-quality dataset for the most promising 240 dynamically stable structures, for which we calculate spectral functions, superconducting bandgaps, and isotropic Migdal-Eliashberg critical temperatures. For 110 of these, we also provide anisotropic Migdal-Eliashberg superconducting gaps and critical temperatures. The approach is remarkably successful in finding known superconductors, and we find 24 unknown ones with a predicted anisotropic T_c above 10 K. Among them, we identify a possible double gap superconductor (p-doped BaB₂), a non-magnetic half-Heusler ZrRuSb, and the perovskite $TaRu_3C$, all exhibiting significant T_c . Finally, we introduce a sensitivity analysis to estimate the robustness of the predictions.

Keywords: Superconductivity, high-throughput, electron-phonon, BCS, Migdal-Eliashberg, first-principles

¹PSI Center for Scientific Computing, Theory, and Data, and National Centre for Computational Design and Discovery of Novel Materials (MARVEL), 5232 Villigen PSI, Switzerland.

²European Theoretical Spectroscopy Facility, Institute of Condensed Matter and Nanosciences, Université catholique de Louvain, Chemin des Étoiles 8, 1348 Louvain-la-Neuve, Belgium.

⁶Bremen Center for Computational Materials Science, and MAPEX Center for Materials and Processes, University of Bremen, 28359 Bremen, Germany.

⁷Theory and Simulation of Materials (THEOS), and National Centre for Computational Design and Discovery of Novel Materials (MARVEL), École Polytechnique Fédérale de Lausanne (EPFL), 1015 Lausanne, Switzerland.

⁸Department of Quantum Matter Physics, University of Geneva, 24 Quai Ernest-Ansermet, 1211 Geneva, Switzerland.

^{*}marnik.bercx@psi.ch, ** samuel.ponce@uclouvain.be.

Introduction

Superconductors play an important role in many modern technologies, finding applications in magnetic resonance imaging machines, maglev trains and large-scale research infrastructures such as the large-hadron collider at CERN. Over the past century, many classes of materials have been identified as new potential superconductors, but the most commonly used ones are still Nb-Ti alloys and A15 phases such as Nb₃Sn [1] which are well described by the Bardeen-Cooper-Schrieffer (BCS) theory of superconductivity [2]. Hightemperature superconductors such as cuprates [3] and iron-based [4] superconductors have much higher transition temperatures (T_c) but often come with challenges that hinder their practical use, such as brittleness, anisotropic superconductivity requiring precise grain alignment, and low critical currents, not to mention a still elusive theoretical foundation. Until the last century, around one hundred stoichiometric, ambient pressure, BCS superconductors had been found [5], representing only one (on average) new superconductor every year since the discovery of superconductivity, with most recent efforts delivering near room temperature critical temperatures, albeit at ultra-high pressures [6]. Despite extensive efforts, targeted or serendipitous discoveries have not fulfilled the demand for high-performance superconductors for industrial and scientific applications, and a cost-effective computational search is also desirable.

During the past few decades, first-principles calculations have played an increasingly important role in both understanding and predicting the material-specific aspects of superconductivity; see, e.g., Ref. [2] for a review. Although understanding high-temperature superconductivity is still challenging [7], conventional BCS superconductors are typically tractable and can be studied readily via well-established techniques [8, 9]. Therefore, a number of efforts have recently emerged to find new phonon-driven superconductors using abinitio evolutionary search [10], machine learning approaches [11-13] or high-throughput screening [11, 14, 15]. Machine learning approaches are often based on training on the experimental SuperCon database [5], which contains chemical formulae but not the crystal structures and focuses primarily on non-conventional superconductors. Instead, high-throughput studies based on first-principles calculations have relied on coarse momentum grid integrations for screening and performed accurate calculations on a small number of promising candidates. As shown before [16] and also highlighted here, a precise calculation of the electron-phonon interactions, essential for determining superconductivity, typically requires an ultra-dense sampling of the Brillouin zone.

The EPW (Electron-phonon using Wannier functions) code [17, 18] can perform such precise interpolations of the electron-phonon matrix elements at a low computational cost. However, performing an extensive search using these advanced methods remained elusive until now, as obtaining the relevant maximally-localized Wannier functions (MLWFs) [19] historically required a combination of chemical intuition and trialand-error efforts. In this work, we combine recent developments in automated Wannierization algorithms [20] with the AIIDA computational infrastructure [21] to perform a systematic and reproducible screening of the Materials Cloud 3D database (MC3D) [22] for BCS superconductors. Importantly, the MC3D has been obtained combining three crystal-structure databases (COD [23], ICSD [24] and MPDS [25]), filtering out as much as possible entries that are not backed by experimental results, and keeping only stoichiometric compounds at standard conditions. The goal here is to explore with stateof-the-art electronic-structure calculations known materials for novel properties, in the same spirit as Mounet et al. [26], rather than predicting novel materials (with all the challenges that it entails for novel properties [27]). Starting from a set of 4533 non-magnetic metals (as predicted from Kohn-Sham DFT, that underestimates band gaps), we first perform an initial screening at progressively higher levels of precision. Based on these results, we select the top 949 materials for which we perform full electron-phonon interpolations. Out of these, we exclude 47 materials found to be magnetic after an additional test, 359 materials due to calculation failures, 270 showing unstable phonon modes, and 33 due to an insufficient quality in the interpolated band structures. From the remaining 240 promising candidates, we compute Wannier functions, Eliashberg spectral

functions $\alpha^2 F(\omega)$ and the isotropic Migdal Eliashberg superconducting $T_{\rm c}^{\rm iso}$. Finally, for the 157 materials with a T_c larger than 5 K, we perform a full anisotropic Migdal-Eliashberg superconducting calculation. These final calculations are memory intensive and 47 fail for this reason, leaving a final set of 110 anisotropic T_c^{aniso} predictions. For each material, our database, available openly on the Materials Cloud Archive [28] and presented in the Supplemental Material, reports electronic band structures and phonon dispersions, Eliashberg spectral functions $\alpha^2 F(\omega)$, Allen-Dynes T_c [29], isotropic and anisotropic Migdal-Eliashberg superconducting gaps $\Delta_{n\mathbf{k}}$ and $T_{\rm c}$ [16]. To our knowledge, this effort represents the largest database of converged anisotropic superconducting Migdal-Eliashberg calculations.

From the list of 240 $T_{\rm c}^{\rm iso}$ candidates, we find that 137 of them are known superconductors with a $T_{\rm c}$ in reasonable agreement with experiment. The remaining 103 compounds are not known to be superconducting, and 24 of these have a predicted $T_{\rm c}$ above 10 K. To ensure the robustness of these predictions with respect to the (approximate) Kohn-Sham band structures and position of the Fermi energy (that in experiments can be affected by defects and unintentional doping or self-doping), we introduce a sensitivity criterion based on homogeneous doping within the rigid band approximation. We then discuss in detail three appealing examples: the hole-doped twogap superconductor BaB₂, the potentially first half-Heusler superconductor ZrRuSb, and the perovskite TaRu₃C.

Results

Screening of the MC3D database and high-throughput calculations

We start our screening from a set of Crystal-lographic Information File (CIF) files extracted from 3 databases available in the literature: MPDS [25], ICSD [24], and COD [23]. These have been analyzed extensively by us and combined into a database of unique, experimentally known structures at ambient conditions. Subsequently, each structure has been optimized with DFT calculations following a strict protocol after initializing them in a high-spin ferromagnetic state to identify magnetic materials. The optimized

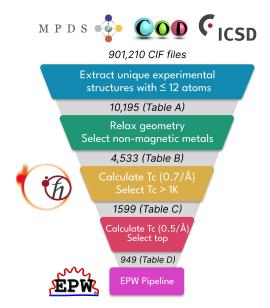


Fig. 1: Initial screening of experimentally known materials. The structures are extracted from the MPDS [25], COD [23], and ICSD [24] databases using the QUANTUM ESPRESSO electron-phonon coupling workflow. Table A, B, C, and D correspond to the full list of materials belonging to each category and published with this work [28].

geometries are published as the Materials Cloud 3D database (MC3D) [22], whose details are provided in Supplementary Sec. 1. Starting from the MC3D, non-magnetic materials with 12 atoms or less in the primitive unit cell are considered (see Fig. 1). Finally, metals are selected based on the Fermi level and occupations at the Kohn-Sham DFT level, leading to 4533 compounds that we screen for potential superconductivity.

Next, we calculate the electron-phonon interactions using density-functional perturbation theory as implemented in the QUANTUM ESPRESSO distribution [30]. In our initial screening, we created a workflow to calculate the Eliashberg spectral function and corresponding Allen-Dynes $T_{\rm c}^{\rm AD}$, progressively increasing the precision of the calculations by using denser and denser phonon (**q**) and commensurate electron (**k**) sampling grids. In the first step, we use a coarse homogeneous **q**-point grid with density $0.7~{\rm \AA}^{-1}$ and identify structures with a $T_{\rm c}^{\rm AD}$ above 1 K as potential superconductors. In the second iteration, a **q**-point grid with density $0.5~{\rm \AA}^{-1}$ is

used from which we make a selection of the 949 structures with the highest $T_{\rm c}$ (see the Methods section for details on the workflow). While this initial screening, based on the linear interpolation approach of Wierzbowska et al. [31], is a solid first step to detect materials as superconductors, a significant number of structures have a $T_c^{\rm AD}$ that is not yet converged with respect to sampling (see Supplementary Sec. 2). Since denser grids are computationally prohibitive and the Allen-Dynes approximation to the T_c has limited accuracy [16], in the final step of our screening we use the EPW code [17, 18] to interpolate electron-phonon matrix elements on ultra-dense grids at low computational costs. Thus, we take the top 949 candidates with the goal of first calculating the isotropic Eliashberg $T_{\rm c}$ using the EPW code (see Fig. 2).

Since magnetism aligns spins in a particular direction, it breaks the spin-singlet pairing of Cooper pairs [32] and is detrimental to standard superconductivity. We therefore first perform both a non-magnetic and ferromagnetic structural relaxation of all the materials to determine if the ferromagnetic solution is more stable (in order to discard it), resulting in a set of 893 nonmagnetic metals. To perform the interpolations with EPW, we rely on the SCDM-k method [20] to automatically generate maximally-localized Wannier functions that span the occupied and lowest unoccupied bands, and that act as an essentially exact interpolator of the Kohn-Sham band structures [19]. In the coarse grid calculations required to set up the Wannier interpolations, the workflows for 285 compounds failed, mostly due to issues related to reaching computational convergence or resource limits (out-of-memory errors or time limits). For the remaining 608 coarse grid calculations, we interpolate the phonon band structure and apply an acoustic sum rule that enforces the 15 Born-Huang conditions [33] and then check the dynamical stability of the structure.

At this stage we exclude 6 materials due to non-Hermiticity of the dynamical matrices due to the dipole-dipole interatomic force constant ansatz [34]; for the 602 interpolated phonon dispersions, we find that 238 have soft modes away from Γ which indicates potential instabilities. We also find 99 structures with soft modes at Γ that we try to stabilize by applying a random perturbation of the atomic positions and relaxing the

geometries; this allows us to stabilize a further 15 structures. For the remaining 280 materials, we assess the quality of the Wannier functions interpolation by comparing an electronic band structure directly calculated with DFT and the interpolated one, accepting a maximum 50 meV weighted band distance [35]. This leads us to 242 structures that are dynamically stable and have accurate Wannier interpolations of the electronic band structure. These are then passed to the superconductivity workflow (see Fig. 2), which performs an automatic convergence of the interpolation mesh based on $T_{\rm c}^{\rm AD}$. Once $T_{\rm c}^{\rm AD}$ is found to converge within 1 K, another run is performed to calculate the isotropic Eliashberg critical temperature T_c^{iso} with the corresponding interpolation mesh. During this automatic convergence of the interpolated momentum meshes, we exclude 2 materials due to convergence issues, which leaves 240 materials for which we perform a converged $T_{\rm c}^{\rm iso}$ calculation. For the 157 structures that have a $T_{\rm c}^{\rm iso}$ above 5 K we perform a final anisotropic Eliashberg T_c^{aniso} calculation to obtain the superconducting gap $\Delta_{n\mathbf{k}}(T)$ on the Fermi surface. During the anisotropic Eliashberg calculations, 47 materials failed due to out-of-memory error or reaching execution time limits, leading to a final set of 110 high-quality, tightly converged anisotropic Eliashberg results. Additional details on the EPW workflow are provided in the Methods section.

Analysis of the supercond-EPW database

The resulting database of structures and properties, called *supercond-EPW*, contains the primitive unit cells, electronic band structures, phonon dispersions, Eliashberg spectral functions $\alpha^2 F(\omega)$, $T_{\rm c}^{\rm AD,f}$ on the fine grid, and $T_{\rm c}^{\rm iso}$ for 240 metals. For 110 of these having a $T_{\rm c}^{\rm iso}$ > 5 K, we also provide the T_c^{aniso} and $\Delta_{n\mathbf{k}}(T)$. These results are reported in Supplementary Sec. 7 and on the Materials Cloud Archive [28]. To understand which of the structures among these candidates are known superconductors, we perform an extensive literature survey and search for reported critical temperatures. We find that 137 out of 240 materials have been experimentally investigated for their critical temperature and, for 76 of them where the structure and not only the chemical formula are reported, we can confirm that

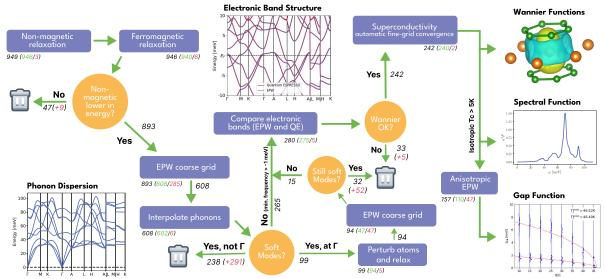


Fig. 2: Flowchart of the Electron-Phonon Wannier (EPW) workflow. The pipeline starts from the top candidates obtained from the initial QUANTUM ESPRESSO screening. The numbers below each of the components of the pipeline indicate the number of materials that were run, with successful runs in green and failed runs in red between the brackets. When structures are discarded along the pipeline, the number of failed structures is also indicated in red between the brackets in addition to the number of discarded structures due to magnetism, the presence of soft modes or insufficient quality of the Wannierization.

the experimental structure matches the calculated one, see Supplementary Sec. 7. From these, 6 are false positives (not superconducting down to 2 K). This means 70 (92%) of the structures for which we have a confirmed experimental result are true positives, which is a strong indication that our procedure can reliably identify superconducting materials from a large pool of initial candidates. To assess the risk of eliminating materials erroneously (false negatives), we extracted a list of 32 well-known superconductors from the literature and investigated how many of these are discarded by our procedure (see Supplementary Sec. 3). From these, we missed seven; these include three failures in the phonon calculation (which could be resolved in future improvements of the workflows to make them more robust), and two due an insufficient interpolation quality of the band structure (an issue that can be resolved via improved approaches to automated Wannierization using projectability disentanglement [36]). Finally, we find that the remaining two cases are due to the presence of soft modes in the phonon dispersions. We highlight the particular case of δ -NbN with an experimental T_c of 16 K [37] that was discarded due to soft modes at the $\mathbf{q} = \mathbf{X}$ point, the reason

being that the experimental δ -NbN can only be prepared with a small N deficiency and that it has been found that disorder can be simulated with a large electronic smearing [38].

In Table 1, we list the top 30 compounds for which we have an experimental result and a matching structure, with the highest T_c^{iso} , along with the corresponding $T_{\rm c}^{\rm AD}$ temperatures for the coarse and fine grid, $T_{\rm c}^{\rm aniso}$ and reported experimental value. In the list, several classes of well-known superconductors are present, such as elemental Nb and Tc, MgB₂, and the A15 phases (Nb₃Sn and Mo₃Os). However, we also note some of the false positives mentioned above, RuO₂ and TaB_2 , which have a high calculated T_c , yet experimental reports indicate that they are not found to be superconducting. Moreover, in some cases we find a large discrepancy between the reported experimental critical temperature and the calculated ones. These results indicate that comparing computational predictions with experimental data presents certain challenges. These include (i) the limited availability of comprehensive databases, (ii) uncertainties in the structures present in experiments, and (iii) the presence of material complexities such as doping, grain boundaries,

Table 1: Top 30 compounds that are known superconductors. From the screening the list is ordered according to the computed $T_c^{\rm aniso}$, together with chemical formulae, space group number, Allen-Dynes transition temperature ($T_c^{\rm AD,c}$ in K) computed with direct coarse grids, Allen-Dynes transition temperature ($T_c^{\rm AD,f}$ in K) interpolated on fine grids, isotropic Eliashberg transition temperature ($T_c^{\rm iso}$) in K, anisotropic Eliashberg transition temperature ($T_c^{\rm aniso}$) in K, and experimental T_c . All the predicted T_c are obtained with an effective Coulomb potential of $\mu^* = 0.13$, a reasonable assumption for many experimentally verified superconductors. All experimental references and full details of the structures and properties are provided in Supplementary Sec. 7.

Material	$T_c^{\mathrm{AD,c}}$	$T_c^{\mathrm{AD,f}}$	$T_c^{\rm iso}$	$T_c^{\rm aniso}$	Experimental T_c
$MgB_{2}-191$	25.6	12.3	16.5	40.8	39.0
MoN-187	23.7	26.7	32.1	36.6	4.0 - 6.0
$Nb_3Sn-223$	11.8	18.7	25.6	35.6	17.9 - 18.3
RuO_2 -136	11.9	21.9	26.1	34.0	< 0.3
PdH-225	30.0	21.2	25.9	30.1	8.5-11.0
V-229	19.0	20.4	27.1	29.1	4.7 - 5.1
$TaSe_2-194$	4.1	9.8	20.1	27.5	0.1
$NbSe_2-194$	5.8	16.4	21.9	26.8	5.7
MoC-194	22.3	17.3	20.8	25.5	8.0
V_3 Pt-223	10.2	14.9	18.5	25.2	3.0
TaS_2-194	4.7	16.7	21.8	25.0	0.5 - 2.2
VC-225	18.9	17.2	20.7	25.0	1.8
$NbS_{2}-194$	8.5	18.6	24.3	24.8	6.1
$TaB_{2}-191$	14.4	15.5	17.5	21.6	< 1.5
$Ta_3Sn-223$	9.4	11.6	15.6	21.6	5.6
Nb-229	13.1	15.2	19.7	21.2	9.2
$Mo_3Os-223$	16.3	15.4	18.9	20.8	7.3 - 12.7
$CaC_{6}-166$	10.5	11.6	12.1	19.1	11.5
ZrN-225	10.3	9.8	12.6	18.6	9.3-9.6
ZrRuP-189	8.2	13.1	15.9	17.9	13.0
YCI-12	4.9	8.5	13.6	17.7	11.8
$ZnNi_3N-221$	8.4	14.6	18.3	17.6	3.0
Tc-194	11.9	12.8	16.3	17.1	7.9
YCCl-12	3.9	7.3	12.0	14.6	2.3
TiN-225	10.3	9.9	12.9	14.1	5.5
$NbB_{2}-191$	9.0	10.6	13.0	13.8	9.4
HfN-225	10.4	9.7	11.7	13.8	5.8
$BaGe_3-194$	2.5	8.7	10.9	13.2	4.0 - 6.5
ScSe-225	5.0	8.0	10.0	12.3	3.7
Sn-139	4.9	8.0	11.0	11.6	3.7

defects, strain, off-stoichiometries, or site-antisite mixing, all of which can significantly influence $T_{\rm c}$ and may not be captured by state-of-the-art computational methods. On the computational side, the most significant approximation is the use of Kohn-Sham band structure; DFT is not a spectral

theory, and more expensive many-body perturbation theory should be employed to calculate electronic excitations [39].

In Table 2, we report the top 30 experimentally known compounds that are predicted by the workflows discussed here to be BCS superconductors. We note that VC, CrH, and Be₂B have also been reported as superconductors in the computation work of Choudhary et al. [11], with predicted T_c of 28.1 K, 10.7 K, and 8.8 K, respectively. These values are in good agreement with the 20.7 K, 13.4 K, and 10.9 K isotropic $T_{\rm c}$ that we compute. In addition, W_2N_3 monolayer [40] and $TaMo_2B_2$ [41] have also been proposed theoretically with predicted T_c of 21 K and 12 K, respectively. The other materials presented in Table 2 are novel in the sense that they have never been reported as superconductors. However, many materials in the list contain heavy elements with partially occupied d or fshells and could be magnetic, even if the initial screening found them to be non-magnetic. Henceforth, we additionally validate all transition-metal compounds in Table 2 employing state-of-the-art self-consistent relaxations using on-site and intersite Hubbard correction [42] for the materials in their nonmagnetic and ferromagnetic configurations, using the HP code [43] to determine U and V from first-principles. The Hubbardcorrected band structure of the materials and their magnetic energy landscape is reported in Supplementary Sec. 4 and the materials with a ferromagnetic ground state are noted in Table 2. Since magnetism is detrimental to BCS superconductivity [32], all results are reported for materials in their PBE nonmagnetic ground state.

Overall, the material with the highest predicted T_c^{aniso} is BaB₂, which displays interesting two-gap superconductivity, reminiscent of the well-known behavior observed in isostructural and isoelectronic MgB₂. [44]. One could wonder how such a simple binary material had not been discovered already. As discussed in the next section, we find that pristine BaB_2 displays a small instability and relaxes to a different structure than the experimentally reported one. However, upon p-doping of 0.065 holes per unit cell, the MgB₂-like phase stabilizes and shows high promise. Despite these results, careful consideration is necessary since DFT electronic band structure and Fermi level position are inexact [45]. We therefore introduce a sensitivity analysis for the predictions, which

Table 2: Top 30 compounds from this screening that are predicted to be BCS superconductors. Largest T_c (K) for materials predicted to be BCS superconductors, following the same convention as Table 1. For $T_c^{\rm AD,f}$ and $T_c^{\rm iso}$ we provide a sensitivity analysis which gives the change of T_c upon homogeneous electron (superscript) and hole (subscript) doping of 10^{21} cm⁻³. Materials that have a potentially magnetic ground state based on self-consistent Hubbard calculations, or for which we could not confirm the structure or source, are noted. BaB₂ is listed separately, as a hole doping of 0.065 holes per unit cell is required to stabilize the phase.

pirase.							
Material	$T_c^{ m AD,c}$	$T_c^{ m AD,f}$	T_c^{iso}	$T_c^{\rm aniso}$			
W_2N_3-194	11.3	$20.3^{+0.6}_{-0.9}$	$26.3^{+0.6}_{-1.0}$	33.7			
$\mathrm{Be_2B}\text{-}225$	9.7	$7.7_{-0.3}^{+0.5}$	$10.9^{+0.7}_{+0.2}$	22.1			
PtO-131	8.9	$13.3^{+0.1}_{-0.1}$	$16.3^{+0.3}_{-0.2}$	19.5			
$Mo_3Be-223$	9.3	$8.1^{+0.4}_{-0.4}$	$10.5^{+0.4}_{-0.4}$	17.6			
TeAs-225	6.4	$10.6^{+0.5}_{-0.4}$	$13.8^{+0.6}_{-0.6}$	17.2			
${\it TaCoSb-216}$	11.4	$11.4^{-0.7}_{-2.7}$	$14.1^{-0.7}_{-3.6}$	16.8			
TaS-187	8.4	$9.3^{-0.8}_{+0.0}$	$11.3^{-1.0}_{-0.6}$	13.7			
YIr_3B_2 -12	6.2	$4.8^{-0.2}_{+0.2}$	$8.6^{-0.3}_{+0.3}$	12.3			
ZrRuSb-216	5.1	$8.9^{+0.5}_{-0.7}$	$9.9^{+0.5}_{-0.9}$	11.1			
HfRuSb-216	3.8	$4.9^{+0.5}_{-0.5}$	$6.6^{+0.6}_{-0.6}$	8.7			
$Zr_2Al-140$	3.0	$5.7^{+0.2}_{-0.2}$	$7.4^{+0.4}_{-0.0}$	7.8			
MoB-63	3.9	$4.8^{-0.1}_{-0.1}$	$6.8^{-0.1}_{-0.1}$	7.7			
	Potentially magnetic						
TaRu ₃ C-221	15.0	$16.5^{-1.9}_{+1.4}$	$21.0^{-2.6}_{+4.4}$	25.0			
$NbRu_3C-221$	15.6	$17.5^{-1.5}_{+1.2}$	$21.8^{-2.0}_{+1.7}$	24.9			
NbCoSb-216	12.4	$16.3^{-1.5}_{+1.0}$	$20.4_{+1.4}^{-1.7}$	21.4			
IrS_2 -205	12.6	$13.2^{-0.3}_{-0.0}$	$16.1^{-0.3}_{-0.0}$	20.8			
ZrS-129	10.9	$10.7^{+0.0}_{-0.1}$	$13.4^{-0.3}_{-0.2}$	18.8			
${ m Ti}_3{ m SnH-221}$	7.9	$11.7^{-1.4}_{-0.3}$	$14.6^{-2.8}_{-1.4}$	18.7			
RhS_2 -205	16.6	$9.4^{-0.6}_{+1.0}$	$11.8^{+0.5}_{+0.7}$	17.3			
CrH-225	9.8	$10.6^{-0.2}_{+0.3}$	$13.4^{-0.2}_{+0.3}$	16.9			
TiRuSb-216	7.5	$10.1^{+0.7}_{-1.0}$	$12.9^{+1.1}_{-1.9}$	13.5			
RhSe-194	7.7	$8.3^{-1.1}_{+1.0}$	$10.8^{-1.6}_{+0.8}$	11.4			
$\mathrm{Ti_{2}Ga}$ -194	3.9	$5.2^{+0.1}_{-0.2}$	$7.1^{-0.1}_{-0.4}$	8.4			
		Unconfirmed source					
YC-225	15.4	$13.4^{+0.7}_{-0.9}$	$17.1^{+1.0}_{-0.9}$	21.9			
$\mathrm{TaMo_2B_2\text{-}127}$	9.5	$9.7^{-0.7}_{+0.6}$	$12.1_{+0.5}^{-0.8}$	14.3			
$\rm Zr_3Sn\text{-}223$	8.8	$7.7^{-0.3}_{+0.3}$	$9.9^{-0.3}_{+0.2}$	14.2			
$\rm LiAl_2Ge\text{-}225$	3.8	$8.0^{+0.1}_{-0.0}$	$9.7^{+0.1}_{-0.1}$	10.9			
$\text{Li}_2 \text{AlGe-} 216$	6.2	$5.8^{+0.3}_{-0.2}$	$7.3^{+0.3}_{-0.2}$	10.0			
AgF_2 -14	8.1	$5.1_{+1.0}^{-0.7}$	$6.7^{-1.4}_{+0.5}$	8.0			
	Hole-doped stabilization						
BaB ₂ -191	20.4	$21.4^{+0.2}_{-0.1}$	$33.0^{+0.3}_{-0.2}$	61.6			

consists in computing the change of Allen-Dynes $T_{\rm c}$ and isotropic $T_{\rm c}$ upon a homogeneous electron (+) and hole (-) doping of 10^{21} cm⁻³. This doping corresponds to a medium/high metallic doping that can realistically be achieved through substitution or interstitial doping (through ion implantation, the Fermi level can be experimentally fine-tuned at meV level to achieve the optimal doping to enhance the superconducting critical temperature [46]). Doping levels above 10^{22} cm⁻³ are usually not feasible due to potential phase segregation [47]. We translate the doping density into energy shifts around the Fermi level, where changes of T_{α} can be evaluated via the Eliashberg equations (see Supplementary Sec. 5 for a detailed description). We report in Table 2 this sensitivity analysis and find 13 superconductors for which $T_{\rm c}$ changes by less than 0.5 K upon $\pm 10^{21}$ cm⁻³ doping, and thus can be considered more robust with respect to the predictions.

An interesting class of structures in Table 2 are the half-Heusler compounds NbCoSb, TaCoSb, TiRuSb, ZrRuSb, and HfRuSb [48]. Many properties of Heusler compounds, including the electronic structure, are typically related to their valence electron count (VEC). Half-Heusler is one of the most common structure types for ternary intermetallics, and commonly half-Heusler phases have a VEC of 8, 18, or 28 per formula unit, corresponding to a closed-shell configuration. Therefore, half-Heusler phases are typically semiconducting, whereas the few openshell half-Heusler phases are typically metallic in nature [49]. Although many examples of full-Heusler superconductors have been discussed in the literature, both in experimental [50] and computational [51] work, superconductivity in half-Heuslers is found to be non-conventional [52, 53] or topological in nature [54] and related to their noncentrosymmetric structure [55]. For full-Heusler phases, Graf et al. [50] have proposed a relationship between the VEC and superconducting properties, citing a prevalence of superconducting full Heuslers with VEC 27. For TiRuSb, HfRuSb, ZrRuSb, NbCoSb, and TaCoSb the VEC is 17 and 19, indicating an electron deficiency and surplus compared to VEC 18, respectively. Reports on conventional superconductivity in half-Heusler compounds are scarce, making this an exciting avenue for further exploration. There are also several perovskite structures in the list, including

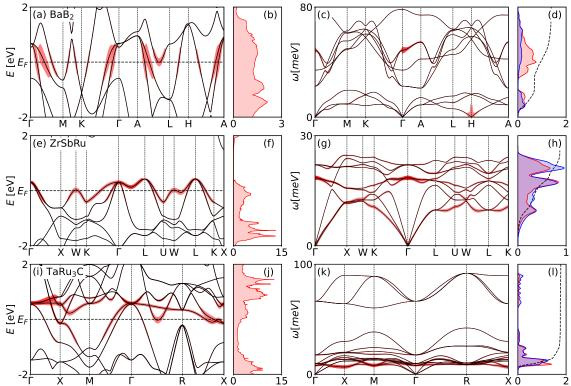


Fig. 3: Analysis of electronic, vibrational, and electron-phonon properties of BaB₂, ZrSbRu, and TaRu₃C. Electron band structures, electron density of states, phonon dispersions, spectral functions (red), accumulated spectral functions (black dashed) and phonon density of states (blue) for doped-BaB₂ (a-d), ZrRuSb (e-h) and TaRu₃C (i-l). The band-resolved electron-phonon coupling constant $\lambda_{n\mathbf{k}}$ and mode-resolved electron-phonon coupling constant $\lambda_{q\nu}$ are plotted on the band structures and phonon dispersion as proportional to the linewidth. The largest band-resolved coupling constants are 2.82, 1.11, 3.16, respectively.

 ${
m TaRu_3C}$, ${
m ZnNi_3N}$, ${
m NbRu_3C}$, ${
m Ti_3TlN}$ and ${
m Ti_3SnH}$, where ${
m TaRu_3C}$ has the highest predicted $T_c^{
m aniso}$ of 25.0 K. Perovskites [56] and antiperovskites [57] are well-known families of superconductors where empirical relations exist between T_c and cation charges in the perovskites cages [58].

Analysis of BaB_2 , ZrSbRu, and $TaRu_3C$

In this section, we focus specifically on BaB₂, the ZrRuSb half-Heusler, and TaRu₃C, as these constitute interesting candidates. Figures 3 and 4 show their electronic and vibrational properties, spectral function, isotropic and anisotropic superconducting gap function $\Delta_0(i\pi T)$ and $\Delta_{n\mathbf{k}}(i\pi T)$. For the anisotropic gap function, we show the histogram of the superconducting gap function $\rho(\Delta)$ at the lowest Matsubara frequency $\Delta_{n\mathbf{k}}(i\pi T)$,

defined as [9]

$$\rho(\Delta(T)) = \sum_{n\mathbf{k}} \delta(\Delta_{n\mathbf{k}}(i\pi T) - \Delta(T))\delta(\epsilon_{n\mathbf{k}} - \epsilon_{F}),$$
(1)

where $\epsilon_{\rm F}$ is the Fermi level. The temperature-dependent isotropic gap $\Delta_0(T)$ and anisotropic gap $\Delta_{n{\bf k}}(i\pi T)$ are fitted by the BCS-type gap function $\Delta^{\rm BCS}(T) = \Delta^{\rm BCS}(0)\sqrt{1-(T/T_c)^\beta}$. To further analyze the structure of electron-phonon coupling, we compute the mode-resolved and band-resolved coupling constants $\lambda_{{\bf q}\nu}$ and $\lambda_{n{\bf k}}$.

We start with a closer investigation of BaB₂, which is an isostructural and isoelectronic counterpart of the well-known two-gap superconductor MgB₂ that was experimentally discovered more than two decades ago [44]. Although BaB₂ has been investigated in the context of superconductivity [59], its critical temperature has never been

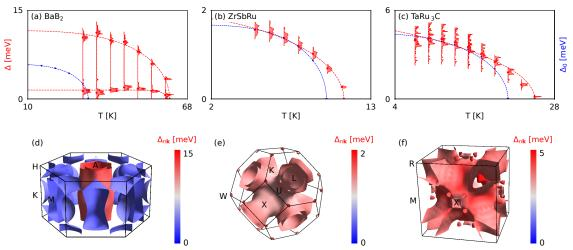


Fig. 4: Analysis of superconducting properties of BaB₂, ZrSbRu, and TaRu₃C. Isotropic gap functions Δ_0 (blue), histograms of anisotropic gap functions $\rho(\Delta, T)$ (red), superconducting gaps on Fermi surfaces for doped-BaB₂ (10 K) (a,d), ZrRuSb (5 K) (b,e) and TaRu₃C (5 K) (c,f).

determined nor predicted. Based on the results from our high-precision workflow described in Fig. 2, the pristine hexagonal phase is unstable due to a soft mode at the H point. Upon further investigation, we find that homogeneous hole doping above $0.065/\text{u.c.} (1.46 \cdot 10^{21} \text{ cm}^{-3})$ can stabilize the pristine phase while superconductivity remains unaffected up to at least 0.1/u.c. (see Supplementary Sec. 6). Analogously to MgB₂, BaB₂ is a strongly coupled material with $\lambda = 1.39$. From Fig. 3(a-d), one can see that the electron-phonon coupling is highly anisotropic, with a dominant optical phonon mode at Γ and an acoustic mode at H, which is unstable in the undoped structure. The interpolated isotropic transition temperature is $T_c^{\text{iso}} = 32.0 \text{ K}$, larger than the $T_c^{\text{AD}} = 24.4 \text{ K}$. According to Fig. 4(a,d), the Fermi surfaces are composed of two nested cylinders along Γ -A line, with a superconducting gap of 11.54 meV and pockets centered at H, M and K points with a superconducting gap of 1.50 meV. This corresponds to two anisotropic critical temperatures $T_c^{\text{aniso},1}$ =61.6 K and $T_c^{\text{aniso},2}$ =60.6 K, larger than the isotropic approximation due to the strong anisotropy. In Fig. 3(a), the band-resolved coupling strength also shows that the coupling is dominated by the two nested cylindrical Fermi-surface

We continue with the five half-Heusler phases NbCoSb, TaCoSb, HfRuSb TiRuSb, and ZrRuSb studying their magnetic states in more detail.

The magnetic landscape is probed using a random forest search where magnetic configurations are constrained and then relaxed using electronic structure calculations at the PBE and PBE+U level with the ROMEO code [60]. The magnetic search is performed in the conventional supercell (12 atoms) to allow for more complex magnetic states. The algorithm is stopped when the ratio of newly discovered unique states to the number of trials goes below 0.2. We show the magnetic energy landscape for each configuration for the four half-Heuslers in Supplementary Sec. 4 and find that all are non-magnetic at the PBE level and ZrRuSb is the only one that remains non-magnetic also at the PBE+U level. We therefore investigate ZrRuSb further and find that its Fermi surface is composed of a sphere centered at Γ (invisible in Fig. 4(e)), two nested connected neck-like formations at the L points, and small spheres centered at the W points. According to Fig. 3(e,g,h), the electron-phonon coupling is overall isotropic, dominated by the phonon density of states, through enhancement of the optical Γ phonon and acoustic phonons near X and L. The interpolated isotropic and anisotropic transition temperatures are 9.9 K and 11.1 K, respectively. However, we note in the DOS of Fig. 3(f) that the high predicted superconductivity in ZrRuSb comes from the position of the Fermi level being located near a van Hove singularity with a flat band around the W **k**-point. This means that this

prediction might not be robust upon small changes of the Fermi level resulting from DFT inaccuracies or experimental conditions. This is supported by the sensitivity check shown in Table. 2, where ZrRuSb varies by over 1 K upon medium doping level.

Finally, we study the perovskite TaRu₃C as our highest- T_c (potentially magnetic) material from Table 2. Indeed, all these materials are non-magnetic at the DFT level but magnetic at the PBE+U level, which tends to over-stabilize magnetic solutions. For TaRu₃C, we show in Fig. 3(k,l) that only low-energy phonons contribute to the electron-phonon couplings, due to the large phonon density of states at these energies. TaRu₃C also possesses very strong electronphonon couplings, manifested by $\lambda = 1.77$. The Fermi surface in Fig. 4(f) is composed by sphere at Γ (invisible in the figure) and connected neck-like formations at R and really small pockets near X. From Fig. 3(i), we note that the Fermi surfaces at the Γ -R line and R-X lines, although they coupled strongly with the phonons, are really sensitive to the shift of Fermi energy. The T_c^{iso} =21.0 K and $T_c^{\rm aniso}$ =25.0 K indicate the somewhat isotropic nature of this material, which is also shown by the homogeneous Cooper pair density on the Fermi surface in Fig. 4(f). We believe that these three materials discussed here (and many others identified in this study) showcase intriguing new physics that is worth further investigation.

In conclusion, starting from 4533 experimentally known compounds with 12 atoms or less in the primitive unit cell obtained from the Materials Cloud 3D database and determined to be non-magnetic metals at the DFT (PBEsol) Kohn-Sham level, we have performed a high-throughput search for novel superconductors using a combination of the QUANTUM ESPRESSO, Wannier90, and EPW codes. Of the top 240 candidates, 137 have been investigated for superconductivity; for the 76 where we can positively match structures, 70 are also reported as superconductors, giving a 92% ratio of true positives and demonstrating the ability of our approach to flag materials as potential superconductors. Of the remaining 103 that have so far not been reported in the experimental literature, we have 24 with a predicted T_c^{aniso} above 10 K. Among the novel candidates, there is the double gap superconductor BaB₂ with a predicted $T_{\rm c}$ of 61.6 K, the half-Heusler ZrRuSb with

a 11.1 K critical temperature, higher than the 12 known full-Heusler superconductors present in our dataset, and the perovskite TaRu₃C with a predicted $T_{\rm c}$ of 25.0 K. If experimentally confirmed, ZrRuSb would be the first half-Heusler superconductors with a VEC of 17 and 19 to exhibit conventional superconductivity. The present results demonstrate the potential of high-throughput calculations to identify new superconductors and provide a valuable resource for future experimental studies, highlighting not only the predictive power of high-throughput calculations but also their limits. Computationally, this work sets the stage for exploring these databases further, including also larger unit cells or higher accuracy methods Wannierization [36] or for electronic band structures, potentially unveiling overlooked superconductors with intriguing physical properties and promising application potential.

Methods

Initial interpolation workflow

Our initial electron-phonon workchain is a workflow that calculates the Eliashberg spectral function based on the linear interpolation approach of Wierzbowska et al. [31]. It consists of the following five steps: (i) a DFT calculation performed on a fine k-point that is used later to perform the linear interpolation, (ii) a second DFT calculation on a coarser grid required to calculate the phonons in the next step, (iii) a phonon calculation which calculates the electron-phonon coefficients on the coarse k-grid with a commensurate q-grid, (iv) the calculations of the real-space force constants, and (v) the Fourier interpolation over a dense **q**-grid and to calculate the final electron-phonon coupling and corresponding spectral function on the fine **k**-point grid.

We use pseudopotentials from the standard solid-state pseudopotentials (SSSP) PBEsol efficiency v1.1 [35] library. For each material, we take the highest value for the plane-wave cutoffs among the suggested values for each of the elements present. We use a k-point grid that is twice the density of the q-grid.

EPW interpolation workflow

The EPW pipeline described in the main text uses several components that run QUANTUM

ESPRESSO in combination with EPW to calculate the electron-phonon coupling and the superconducting critical temperature at a high precision, see Fig. 5 for a schematic representation of the workflow.

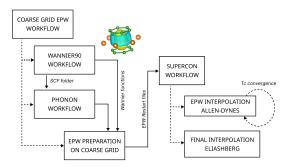


Fig. 5: Schematic of the superconducting workflow. Schematic of the steps executed to obtain the isotropic Eliashberg T_c using the EPW workflows implemented in AIIDA.

The EPW workchain takes care of the coarse-grid Quantum ESPRESSO [30], Wan-NIER90 [61] and EPW [17, 18] calculations that are required for the subsequent interpolations. The workflow consists of the following steps: (i) a first workflow that constructs the Wannier functions for the input structure using the SCDM-k method [20], (ii) a phonon calculation is performed to compute the dynamical matrices and perturbed potentials, and (iii) the input files required for the EPW calculation are converted into the expected format and an EPW calculation is run on the coarse grid to produce the restart files for the interpolation, which are stashed on the remote machine in a permanent location. For the EPW pipeline, we switch to the norm-conserving PBE pseudopotentials from the scalar-relativistic table of Pseudodojo v0.5 [62] as projector augmented wave method pseudopotentials have not been extensively tested with the EPW code. For the energy cutoffs, we select the highest hint value for each element and once again take the highest one from the set of atoms contained in each material.

Based on the stashed restart files produced by the first workchain, a second superconducting workchain is run to interpolate the electronphonon coupling on dense momentum grids and calculate the superconducting critical temperature. The main feature of this workflow is that it automatically converges the fine-grid interpolation meshes for both the **k** and **q** points, based on a calculation of the Allen-Dynes critical temperature and a specified threshold (default 1 K). Once at least 3 calculations have been performed in the convergence loop and the Allen-Dynes critical temperature has converged, the workflow runs a final calculation on the fine grid using the full Eliashberg theory to calculate the isotropic Eliashberg critical temperature on the converged fine grid.

Data availability

All data generated or analysed during this study are included in this Article, its Supplementary Information, and the Materials Cloud Archive [28].

References

- [1] Uglietti, D. A review of commercial high temperature superconducting materials for large magnets: from wires and tapes to cables and conductors. Superconductor Science and Technology 32, 053001 (2019). URL http://dx.doi.org/10.1088/1361-6668/ab06a2.
- Boeri, L. Understanding Novel Superconductors with Ab Initio Calculations, 1-41 (Springer International Publishing, 2018). URL http://dx.doi.org/10.1007/ 978-3-319-50257-1_21-1.
- [3] Shen, K. M. & Davis, J. S. Cuprate high- T_c superconductors. *Materials Today* **11**, 14–21 (2008). URL http://dx.doi.org/10. 1016/S1369-7021(08)70175-5.
- [4] Fernandes, R. M., Chubukov, A. V. & Schmalian, J. What drives nematic order in iron-based superconductors? *Nature Physics* 10, 97–104 (2014). URL http://dx.doi.org/ 10.1038/nphys2877.
- [5] Hosono, H. et al. Exploration of new superconductors and functional materials, and fabrication of superconducting tapes and wires of iron pnictides. Science and Technology

- of Advanced Materials **16**, 033503 (2015). URL http://dx.doi.org/10.1088/1468-6996/16/3/033503.
- [6] Zhang, L., Wang, Y., Lv, J. & Ma, Y. Materials discovery at high pressures. Nature Reviews Materials 2 (2017). URL http://dx.doi.org/10.1038/natrevmats.2017.5.
- [7] O'Mahony, S. M. et al. On the electron pairing mechanism of copper-oxide high temperature superconductivity. Proceedings of the National Academy of Sciences 119 (2022). URL http://dx.doi.org/10.1073/pnas.2207449119.
- [8] Giustino, F. Electron-phonon interactions from first principles. Reviews of Modern Physics 89 (2017). URL http://dx.doi.org/ 10.1103/RevModPhys.89.015003.
- [9] Mori, H., Nomoto, T., Arita, R. & Margine, E. R. Efficient anisotropic Migdal-Eliashberg calculations with the intermediate representation basis and Wannier interpolation. URL http://arxiv.org/abs/2404.11528. 2404. 11528[cond-mat].
- [10] Kolmogorov, A. N. et al. New superconducting and semiconducting Fe-B compounds predicted with an ab initio evolutionary search. Physical Review Letters 105 (2010). URL http://dx.doi.org/10.1103/ PhysRevLett.105.217003.
- [11] Choudhary, K. & Garrity, K. Designing high-tc superconductors with BCS-inspired screening, density functional theory, and deep-learning. npj Computational Materials 8 (2022). URL http://dx.doi.org/10.1038/ s41524-022-00933-1.
- [12] Wines, D., Xie, T. & Choudhary, K. Inverse design of next-generation superconductors using data-driven deep generative models. *The Journal of Physical Chemistry Letters* 14, 6630–6638 (2023). URL http://dx.doi.org/10.1021/acs.jpclett.3c01260.
- [13] Pogue, E. A. et al. Closed-loop superconducting materials discovery. npj Computational Materials 9 (2023). URL http://dx.doi.org/

- 10.1038/s41524-023-01131-3.
- [14] Cerqueira, T. F. T., Sanna, A. & Marques, M. A. L. Sampling the materials space for conventional superconducting compounds. Advanced Materials 36 (2023). URL http://dx.doi.org/10.1002/adma.202307085.
- [15] Tran, H., Dam, H.-C., Kuenneth, C., Ngoc Tuoc, V. & Kino, H. Superconductor discovery in the emerging paradigm of materials informatics. *Chemistry of Materi*als (2024). URL http://dx.doi.org/10.1021/ acs.chemmater.4c01757.
- [16] Margine, E. R. & Giustino, F. Anisotropic Migdal-Eliashberg theory using Wannier functions. *Physical Review B* 87 (2013). URL http://dx.doi.org/10.1103/PhysRevB. 87.024505.
- [17] Poncé, S., Margine, E., Verdi, C. & Giustino, F. Epw: Electron-phonon coupling, transport and superconducting properties using maximally localized Wannier functions. *Com*puter Physics Communications 209, 116–133 (2016). URL http://dx.doi.org/10.1016/j. cpc.2016.07.028.
- [18] Lee, H. et al. Electron-phonon physics from first principles using the EPW code. npj Computational Materials 9 (2023). URL http://dx.doi.org/10.1038/s41524-023-01107-3.
- [19] Marzari, N., Mostofi, A. A., Yates, J. R., Souza, I. & Vanderbilt, D. Maximally localized Wannier functions: Theory and applications. Reviews of Modern Physics 84, 1419–1475 (2012). URL http://dx.doi.org/ 10.1103/RevModPhys.84.1419.
- [20] Damle, A. & Lin, L. Disentanglement via Entanglement: A Unified Method for Wannier Localization. *Multiscale Model. Simul.* 16, 1392–1410 (2018).
- [21] Huber, S. P. et al. Aiida 1.0, a scalable computational infrastructure for automated reproducible workflows and data provenance. Scientific Data 7 (2020). URL http://dx.doi. org/10.1038/s41597-020-00638-4.

- [22] Materials cloud 3d database. https://mc3d.materialscloud.org/. Accessed: 2024-06-21.
- [23] Gražulis, S. et al. Crystallography open database (cod): an open-access collection of crystal structures and platform for world-wide collaboration. Nucleic Acids Research 40, D420–D427 (2011). URL http://dx.doi.org/10.1093/nar/gkr900.
- [24] Inorganic crystal structure database (2024). URL http://www.fiz-karlsruhe.com/icsd.html.
- [25] The pauling file exposed through the materials platform for data science https://mpds.io/. (2024). URL http://paulingfile.com.
- [26] Mounet, N. et al. Two-dimensional materials from high-throughput computational exfoliation of experimentally known compounds. Nature Nanotechnology 13, 246–252 (2018). URL http://dx.doi.org/10.1038/s41565-017-0035-5.
- [27] Cheetham, A. K. & Seshadri, R. Artificial intelligence driving materials discovery? perspective on the article: Scaling deep learning for materials discovery. *Chemistry of Materials* 36, 3490–3495 (2024). URL http://dx. doi.org/10.1021/acs.chemmater.4c00643.
- [28] Materials cloud archive. https://archive.materialscloud.org/record/2025.39. Accessed: 2025-03-13.
- [29] Allen, P. B. & Dynes, R. C. Transition temperature of strong-coupled superconductors reanalyzed. *Physical Review B* 12, 905–922 (1975). URL http://dx.doi.org/10. 1103/PhysRevB.12.905.
- [30] Giannozzi, P. et al. Advanced capabilities for materials modelling with Quantum ESPRESSO. Journal of Physics: Condensed Matter 29, 465901 (2017). URL http://dx.doi.org/10.1088/1361-648X/aa8f79.
- [31] Wierzbowska, M., de Gironcoli, S. & Giannozzi, P. Origins of low- and high-pressure discontinuities of t_c in niobium (2005). URL

- https://arxiv.org/abs/cond-mat/0504077.
- [32] Eremin, I. M., Knolle, J. & Moessner, R. Magnetism and Superconductivity, 1–31 (Springer International Publishing, Cham, 2020). URL https://doi.org/10.1007/978-3-030-63101-7_14-1.
- [33] Lin, C., Poncé, S. & Marzari, N. General invariance and equilibrium conditions for lattice dynamics in 1D, 2D, and 3D materials. npj Computational Materials 8 (2022). URL http://dx.doi.org/10.1038/s41524-022-00920-6.
- [34] Gonze, X. & Lee, C. Dynamical matrices, born effective charges, dielectric permittivity tensors, and interatomic force constants from density-functional perturbation theory. *Physical Review B* 55, 10355–10368 (1997). URL http://dx.doi.org/10.1103/PhysRevB.55.10355.
- [35] Prandini, G., Marrazzo, A., Castelli, I. E., Mounet, N. & Marzari, N. Precision and efficiency in solid-state pseudopotential calculations. npj Computational Materials 4 (2018). URL http://dx.doi.org/10.1038/ s41524-018-0127-2.
- [36] Qiao, J., Pizzi, G. & Marzari, N. Projectability disentanglement for accurate and automated electronic-structure Hamiltonians. npj Computational Materials 9 (2023). URL http://dx.doi.org/10.1038/s41524-023-01146-w.
- [37] Shy, Y. M., Toth, L. E. & Somasundaram, R. Superconducting properties, electrical resistivities, and structure of nbn thin films. *Journal of Applied Physics* 44, 5539–5545 (1973). URL http://dx.doi.org/10.1063/1.1662193.
- [38] Babu, K. R. & Guo, G.-Y. Electron-phonon coupling, superconductivity, and nontrivial band topology in nbn polytypes. *Physical Review B* **99** (2019). URL http://dx.doi.org/10.1103/PhysRevB.99.104508.
- [39] Reining, L. The gw approximation: content, successes and limitations. WIREs Computational Molecular Science 8 (2017). URL

- http://dx.doi.org/10.1002/wcms.1344.
- [40] Campi, D., Kumari, S. & Marzari, N. Prediction of phonon-mediated superconductivity with high critical temperature in the two-dimensional topological semimetal w2n3. Nano Letters 21, 3435–3442 (2021). URL http://dx.doi.org/10.1021/acs.nanolett.0c05125.
- [41] Chen, S. et al. High-throughput screening for boride superconductors. *Inorganic Chemistry* 63, 8654–8663 (2024). URL http://dx.doi. org/10.1021/acs.inorgchem.4c00159.
- [42] Timrov, I., Marzari, N. & Cococcioni, M. Self-consistent Hubbard parameters from density-functional perturbation theory in the ultrasoft and projector-augmented wave formulations. *Phys. Rev. B* 103, 045141 (2021). URL https://link.aps.org/doi/10.1103/PhysRevB.103.045141.
- [43] Timrov, I., Marzari, N. & Cococcioni, M. HP – a code for the calculation of Hubbard parameters using densityfunctional perturbation theory. Computer Physics Communications 279, 108455 (2022). URL https://www.sciencedirect. com/science/article/pii/S0010465522001746.
- [44] Nagamatsu, J., Nakagawa, N., Muranaka, T., Zenitani, Y. & Akimitsu, J. Superconductivity at 39 k in magnesium diboride. *nature* **410**, 63–64 (2001).
- [45] Marzari, N., Ferretti, A. & Wolverton, C. Electronic-structure methods for materials design. Nature Materials 20, 736–749 (2021). URL http://dx.doi.org/10.1038/ s41563-021-01013-3.
- [46] DePalma, A. Fast h+-ion implantation enables precise fermi level engineering in quantum materials. MRS Bulletin 49, 1189–1189 (2024). URL http://dx.doi.org/10.1557/s43577-024-00822-6.
- [47] Grovogui, J. A. et al. Implications of doping on microstructure, processing, and thermoelectric performance: The case of pbse. Journal of Materials Research 36, 1272–1284

- (2021). URL http://dx.doi.org/10.1557/s43578-021-00130-8.
- [48] Evers, C. B., Richter, C. G., Hartjes, K. & Jeitschko, W. Ternary transition metal antimonides and bismuthides with MgAgAstype and filled NiAs-type structure. *Journal of Alloys and Compounds* 252, 93–97 (1997). URL http://dx.doi.org/10.1016/S0925-8388(96)02616-3.
- [49] Anand, S. et al. A valence balanced rule for discovery of 18-electron half-Heuslers with defects. Energy & Environmental Science 11, 1480–1488 (2018). URL http://dx.doi.org/10.1039/C8EE00306H.
- [50] Graf, T., Felser, C. & Parkin, S. S. Simple rules for the understanding of Heusler compounds. Progress in Solid State Chemistry 39, 1–50 (2011). URL http://dx.doi.org/10. 1016/j.progsolidstchem.2011.02.001.
- [51] Hoffmann, N. et al. Searching for ductile superconducting Heusler X2YZ compounds. npj Computational Materials 9 (2023). URL http://dx.doi.org/10.1038/s41524-023-01084-7.
- [52] Timm, C., Schnyder, A. P., Agterberg, D. F. & Brydon, P. M. R. Inflated nodes and surface states in superconducting half-Heusler compounds. *Physical Review B* 96 (2017). URL http://dx.doi.org/10.1103/PhysRevB. 96.094526.
- [53] Xiao, H. et al. Superconductivity in the half-Heusler compound TbPdBi. Physical Review B 97 (2018). URL http://dx.doi.org/10. 1103/PhysRevB.97.224511.
- [54] Tafti, F. F. et al. Superconductivity in the noncentrosymmetric half-Heusler compound LuPtBi: A candidate for topological superconductivity. Physical Review B 87 (2013). URL http://dx.doi.org/10.1103/ PhysRevB.87.184504.
- [55] Smidman, M., Salamon, M. B., Yuan, H. Q. & Agterberg, D. F. Superconductivity and spin-orbit coupling in non-centrosymmetric materials: a review. Reports on Progress in

- Physics 80, 036501 (2017). URL http://dx.doi.org/10.1088/1361-6633/80/3/036501.
- [56] Kim, M. et al. Superconductivity in (Ba, K)SbO₃. Nature Materials 21, 627–633 (2022). URL http://dx.doi.org/10.1038/s41563-022-01203-7.
- [57] Hoffmann, N., Cerqueira, T. F. T., Schmidt, J. & Marques, M. A. L. Superconductivity in antiperovskites. npj Computational Materials 8 (2022). URL http://dx.doi.org/10. 1038/s41524-022-00817-4.
- [58] Poole, C. P. Handbook of Superconductivity (Elsevier, 2000). URL http://dx.doi.org/10. 1016/B978-0-12-561460-3.X5000-0.
- [59] Emetere Moses, E. Microstructural and electronics dynamics of barium diboride as a superconductor from first principles. *Results in Physics* **19**, 103658 (2020). URL http://dx.doi.org/10.1016/j.rinp.2020.103658.
- [60] Ponet, L., Di Lucente, E. & Marzari, N. The energy landscape of magnetic materials. npj Computational Materials 10 (2024). URL http://dx.doi.org/10.1038/ s41524-024-01310-w.
- [61] Pizzi, G. et al. Wannier90 as a community code: new features and applications. Journal of Physics: Condensed Matter 32, 165902 (2020). URL http://dx.doi.org/10. 1088/1361-648X/ab51ff.
- [62] van Setten, M. et al. The pseudodojo: Training and grading a 85 element optimized norm-conserving pseudopotential table. Computer Physics Communications 226, 39–54 (2018). URL http://dx.doi.org/10.1016/j.cpc.2018.01.012.

Acknowledgments

We acknowledge financial support from the NCCR MARVEL, a National Centre of Competence in Research, funded by the Swiss National Science Foundation (grant number 205602), as well as the European Centre of Excellence MaX "Materials design at the Exascale" (grant no. 824143). The work is also supported by a pilot access grant

from the Swiss National Supercomputing Centre (CSCS) on the Swiss share of the LUMI system under project ID "PILOT MC EPFL-NM 01", a CHRONOS grant from the CSCS on the Swiss share of the LUMI system under project ID "REGULAR MC EPFL-NM 02", and a grant from the CSCS under project ID mr32. S. P. and Y. Z. acknowledge support from the Fonds de la Recherche Scientifique de Belgique (FRS-FNRS) and T.W011.23 (PDR-WEAVE) and also supported by the Walloon Region in the strategic axe FRFS-WEL-T. M.B. and G.P. gratefully acknowledge support from the SwissTwins project, funded by the Swiss State Secretariat for Education, Research and Innovation (SERI). G.P. gratefully acknowledges support from the Swiss National Science Foundation (SNSF) Project Funding (grant 200021E_206190 "FISH4DIET"), F.v.R acknowledges support from SNSF Eccellenza Funding (grant PCEFP2_194183). L.B. and N.M. gratefully acknowledge support from the Deutsche Forschungsgemeinschaft (DFG) under Germany's Excellence Strategy (EXC 2077, No. 390741603, University Allowance, University of Bremen) and Lucio Colombi Ciacchi, the host of the "U Bremen Excellence Chair Program". Computational resources have been provided by the PRACE award granting access to Discoverer in SofiaTech, Bulgaria (OptoSpin project id. 2020225411), and by the EuroHPC JU award granting access to MareNostrum5 at Barcelona Supercomputing Center (BSC), Spain (Project ID: EHPC-EXT-2023E02-050), and by the Consortium des Équipements de Calcul Intensif (CÉCI), funded by the FRS-FNRS under Grant No. 2.5020.11 and by the Walloon Region, as well as computational resources awarded on the Belgian share of the EuroHPC LUMI supercomputer.

Author information

These authors contributed equally: Marnik Bercx, Samuel Poncé.

Authors and Affiliations

Paul Scherrer Institut (PSI) Center for Scientific computing, theory, and data, Villigen, Switzerland Marnik Bercx, Giovanni Pizzi, and Nicola Marzari

Institute of Condensed Matter and Nanosciences, Université catholique de Louvain, Louvain-la-Neuve, Belgium Samuel Poncé, Yiming Zhang

Department of Energy, Politecnico di Torino, Italy Giovanni Trezza, Eliodoro Chiavazzo

Electronic Components, Technology and Materials (ECTM), TU Delft, The Netherlands Amir Ghorbani Ghezeljehmeidan

Bremen Center for Computational Materials Science, and MAPEX Center for Materials and Processes, University of Bremen, Bremen, Germany Lorenzo Bastonero, Nicola Marzari

Theory and Simulation of Materials (THEOS), EPFL, Lausanne, Switzerland Junfeng Qiao, Nicola Marzari

Department of Quantum Matter Physics, University of Geneva, Geneva, Switzerland Fabian O. von Rohr

Contributions

S.P. and N.M. conceived the project, M.B. and S.P. designed the AiiDA workflows, M.B. performed high-throughput calculations with AiiDA, Y.Z. performed analysis of stability, sensitivity and detailed superconductivity, G.T., A.G.G. and M.B performed literature search, L.B. performed magnetic calculation with PBE+U+V and the ROMEO code, J.Q. helped with the automatic Wannier function generation, F.v.R. provided experimental guidance, S.P., G.P., E.C., and N.M. supervised the work. All authors contributed to the writing of the manuscript.

Corresponding authors

Marnik Bercx and Samuel Poncé

Ethics declarations

$Competing\ interests$

The authors declare no competing interests.